ELSA/ 5-2009

Letter of Intent to the PAC

Commissioning of the BGO-OpenDipole setup at beamline S of ELSA

B. Bantes, H. Dutz, H. Eberhardt, D. Elsner, R. Ewald, K. Fornet-Ponse, S. Goertz, D. Hammann, J. Hannappel, W. Hillert, S. Kammer, Frank Klein, Friedrich Klein, H. Schmieden, T. Schwan
University of Bonn, Physikalisches Institut, Germany

R. Beck, S. Böse, K.-T. Brinkmann, R. Jahn, D. Walther T. Würschig
University of Bonn, Helmholtz Institut für Strahlen- und Kernphysik, Germany

Yu. Beloglazov, A. Gridnev, I. Lopatin, V. Nikonov, D. Novinskiy, V. Sumachev
Petersburg Nuclear Physics Instute, Gatchina, Russia

R. Di Salvo, D. Moricciani
INFN sezione Roma "Tor Vergata", Italy

A. Fantini, C. Schaerf
University of Roma Tor Vergata and INFN sezione Roma "Tor Vergata", Italy

F. Ghio, B. Girolami
Instituto Superiore di Sanità and INFN sezione Roma1, Italy

P. Levi Sandri
INFN Laboratori Nazionali di Frascati, Italy

A. Braghieri, A. Mushkarenkov,[§] P. Pedroni
INFN sezione di Pavia, Italy
([§] *also University of Moscow, Russia*)

G. Giardina, G. Mandaglio, M. Manganaro
University of Messina and INFN sezione Catania, Italy

G. Gervino
University of Torino, Italy

D. Glazier, D. Watts
University of Edinburgh, UK

D. Burdeinyi, V. Ganenko, G. Vashchenko
National Science Center Kharkov Institution of Physics & Technnology, Ukraine

A. S. Ignatov, A. M. Lapik, V. G. Nedorezov, A. A. Turinge
University of Moscow, Russia

B. Krusche, I. Jaegle
University of Basel, Switzerland

Spokespersons: P. Levi Sandri and H. Schmieden
Contact Person: H. Schmieden
e-mail: schmieden@physik.uni-bonn.de

Bonn, June 2, 2009

Beam specifications:

e^- beam	2.4 GeV e^- un-polarized
beam line:	beamline S
beam intensity:	1–10 $\cdot 10^6$ tagged and untagged photons/s
time structure:	continuous beam

Equipment:

BGO-OpenDipole setup at beamline S, unpolarized carbon and LH_2/LD_2 target, unpolarized and polarized photon beam in beamline S.

Abstract

The new experimental BGO-OpenDipole setup will be assembled at the ELSA beamline S during 2009. It consists of the combination of an open-dipole forward spectrometer and the BGO Ball of the former GRAAL collaboration to cover the central angular region. This configuration is ideally suited to investigate the photoproduction of multiparticle final states with mixed charges. It extends the present Crystal-Barrel capabilities significantly towards strangeness and vector meson production, and, due to the trigger capability of the BGO readout, to quasifree production of neutral mesons off the neutron using a deuteron or ^{3}He target. In addition it will allow nucleon polarization measurements in single-meson photoproduction. The main piece of the spectrometer is a large 90 t dipole magnet. Scintillating fiber detectors in front of the magnet and drift chambers behind it enable track and hence momentum reconstruction of charged particles. Combined with the time-of-flight from a large scintillator wall, particle ID is provided, enhanced through an aerogel Cherenkov detector. The BGO Ball detects charged and neutral particles, in particular photons. Moreover, it has high efficiency for neutrons. The whole setup will be taken into operation during the year 2010. Time for hall access is requested for the setup phase in 2009. The commissioning of the subdetectors and of the whole setup requires dedicated beamtimes in 2009 and 2010.

1 Preamble

The present letter-of-intent (LoI) addresses the commissioning of the Open-Dipole (OD) forward spectrometer which was originally introduced to the PAC in the LoI ELSA/4-03. In the course of the preparation and setup of the spectrometer the experiment could be put on a much broader basis than originally anticipated. The most important development was the decision of italian groups of the former GRAAL experiment to complement the spectrometer with their BGO ball which previously was used at the ESRF in Grenoble. An overview of the configuration of open-dipole forward spectrometer and BGO ball, called BGO-OpenDipole, is depicted in Fig. 1. It provides a unique instrumentation to detect complex mixed charged/neutral final states in meson photoproduction with very high resolution. In addition, the full trigger capability, in particular of the BGO ball, yields also access to *pure* neutral final states as, e.g., in η photoproduction off the neutron. The excellent forward acceptance opens the possibility to investigate vector meson production in order to understand the reaction mechanism and the role of resonances. The BGO-OpenDipole setup is probably the only detector worldwide to finally falsify or verify the very questionable (in view of other results over the last years) recent LEPS results in K^+K^- photoproduction ("Θ^+") at comparable kinematics. A major scientific goal is the exclusive photoproduction of $\Lambda(1405)$, tagged through its decay into the $\pi^0\,\Sigma^0$ channel. The intended physics is addressed in more detail in Sec. 2.

Linearly polarized beams will be available already in the commissioning phase. In the present beamline configuration maximum longitudinal electron polarization is obtained at approximately 1.7 GeV. Options to increase this energy are investigated. The tagging magnet had already been used in combination with Crystal-Barrel/TAPS when the detector system was installed with unpolarized target at beamline S. A new tagger focal-plane instrumentation will be built in close cooperation with the Crystal-Barrel collaboration.

The whole detector configuration of open-dipole forward spectrometer and BGO Ball shall be installed at the beamline S of ELSA. This minimizes interferences with the Crystal-Barrel setup which, in combination with the BoFrosT polarized target, continues to take data at beamline E. The commissioning of the BGO-OpenDipole setup and the later experiments are advanced by groups and individuals from Germany (Bonn), Italy (Rome, Frascati, Pavia, Messina, Torino), Russia (Gatchina, Moscow), Switzerland (Basel), the UK (Edinburgh) and Ukraine (Kharkov). It is intended to formally establish a collaboration which will be open for further extension.

The central device of the spectrometer is the large 90 ton dipole magnet which was provided on permanent loan basis by DESY. The gap of the magnet is extended to a height of 84 cm and presently the field is precisely mapped using the special facilities and support of the GSI at Darmstadt. The magnet is complemented by tracking detectors, two multi-layer scintillating fiber detectors in front and eight drift chambers with four different wire-orientation behind, to allow for momentum reconstruction of charged particles bent through the magnetic field. The flight-time determined in a large plastic scintillator array (TOF) enables particle identification. This is enhanced through an aerogel Cherenkov detector. The OD-spectrometer covers the forward angular region of $\Theta_{\rm lab} \simeq 0-12\,(8.2)$ degrees in horizontal (vertical) direction. A 3 cm thick lead plate in the dipole's middle plane will prevent e^+e^- background to spoil the

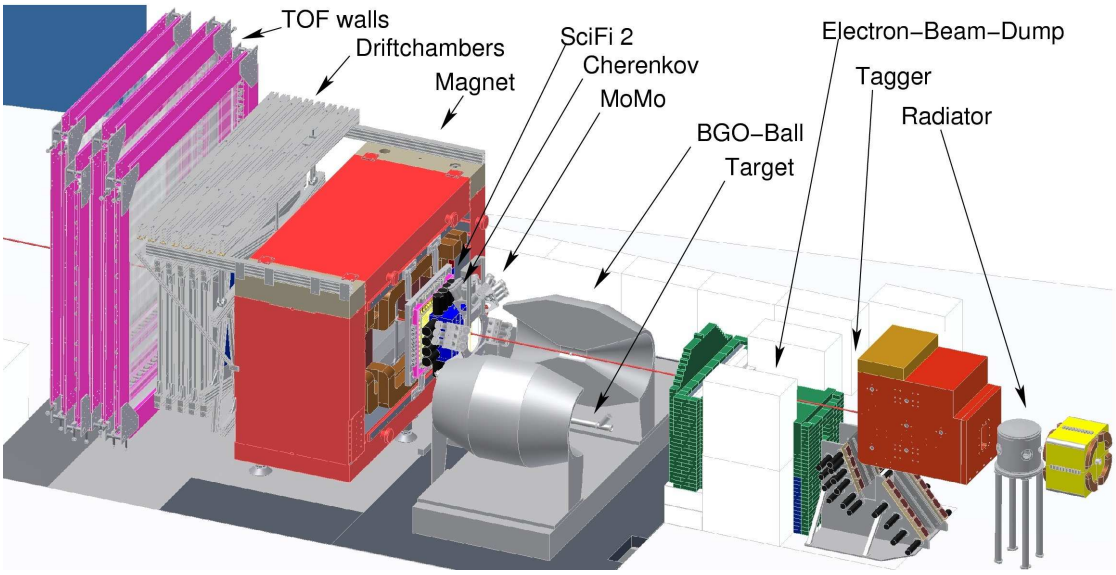

Figure 1: Overview of the detector setup at beamline S.

performance of the drift chambers. The photon beam will be passing through a central bore. In addition, the DCs have a $5 \times 5\,\mathrm{cm}^2$ insensitivity spot to reduce electromagnetic counting load from the photon beam.

The BGO Ball hermetically encloses the target over the polar angular range $25 - 155$ degrees. It is well suited for both, charged and neutral particle detection (including neutrons), distinguished by an internal scintillator barrel. The BGO Ball is equipped with photomultiplier readout providing excellent energy resolution and triggering capabilities.

The BGO-OpenDipole setup is ideally suited for multi-particle final states of mixed charges. Good particle ID is provided, both in the forward region, covered by the large acceptance magnetic spectrometer, and in the central region of the BGO Ball. Especially, in forward direction high resolution is achieved for protons of large momenta. In addition, K^+ and K^- are cleanly identified, also simultaneously, which is important for ϕ photoproduction. The setup enables polarimetry of recoil protons and, as count rates permit, also neutrons. High neutron efficiency is obtained through the combination of BGO [1] (cf. also section 3.2.5) and time-of-flight detector. A particular benefit is the trigger capability of the BGO.

Hence, the BGO-OpenDipole setup is largely complementary to the CB-TAPS setup which is optimized for multiple photon detection and, except for low-energy protons in the forward direction, has rather limited identification capability for charged particles and for neutrons. Distinctive features from the JLab Hall B setup are the high multi-photon acceptance provided by the BGO (see section 3.2.3), and the forward acceptance down to almost 0 degree of the spectrometer. The dipole acceptance is similar to the LEPS setup. However, the combination with the crystal spectrometer makes the BGO-OpenDipole apparatus unique in this comparison as well.

Major parts of the BGO-OpenDipole installation shall be accomplished by the end of 2009 and beginning of 2010. In parallel, the individual subdetectors will be taken

into operation and the commissioning of the whole detector system is subsequently planned during the rest of 2010. The cryogenic LH_2/LD_2 target of the former GRAAL experiment will be available from the beginning. At a somewhat later stage it is foreseen to complement the detector in a threefold way: (i) close the acceptance hole between forward spectrometer and BGO, (ii) extend forward tracking through planar Si-strip detectors for (secondary) vertex reconstruction, and (iii) complement the BGO Ball by an inner cylindric tracking detector (MWPC according to the present planning).

The LoI is organized as follows. The next section provides a rough overview of the physics motivation. Chapter 3 describes the instrumentation and the present status of the individual subdetectors. The intended steps of bringing the whole detector setup into operation are outlined in section 4. The requested setup time without beam – but limited beam availability to the E-area – and the requested setup and test time with beam – and limited access to the E-area – is specified in section 5.

2 Physics motivation

Both, baryon and meson spectroscopy, indicate that the uncorrelated quark model of hadrons is too simple. Correlations on quark or meson-baryon level seem to play a crucial role in hadron structure, may even be dominant in some specific states which are still unsatisfactorily understood in quark models. In the baryonic sector are among those the low-lying $P_{11}(1440)$, the $S_{11}(1535)$ and the $\Lambda(1405)$ states. At higher excitation energies in the 2^{nd} and 3^{rd} resonance region the sheer number of predicted states remains dubious.

The experimental tool to investigate baryon resonances is the photoproduction of mesons. Some channels may exhibit sensitivity to specific states, e.g. ηp to the $S_{11}(1535)$, but in general the different channels are *not* independent. In order to achieve a full understanding of the role of baryonic resonances, it is hence mandatory to investigate "coupled" channels, including non-strange pseudoscalar mesons with different charge combinations, strange and vector mesons. The measurement of as many as possible independent observables is necessary to fully disentangle the reaction mechanisms involved. Beyond the pure necessity for resonance extraction, the reaction mechanisms are interesting in themselves, in particular in strangeness and vector meson production.

Neutral meson channels are less susceptible to physical background when probing s-channel excitations. However, the full picture in the above sense requires charged channels as well. Moreover, vector mesons and hyperons predominantly decay into charged channels. Hence, charged reaction channels are equally important. A special role is played by photoproduction on the neutron: The couplings may differ surprisingly from the proton as recent results in quasifree η photoproduction clearly demonstrated [2, 3, 4].

Some important aspects of the physics program addressed with the BGO-OpenDipole setup are briefly sketched in the following.

η photoproduction

η production is one of the most interesting channels in meson photoproduction: Firstly, the threshold region is strongly dominated by the $S_{11}(1535)$ resonance, one of the low-

lying states with much debated structure. Secondly, the isoscalar nature of the η greatly reduces the complexity of the spectrum of possible s-channel resonance contributions and hence facilitates the search for previously unseen N^* states. Recoil polarimetry is mandatory to achieve a "complete" experiment with respect to an unambiguous extraction of reaction amplitudes. It can be achieved in η photoproduction on the proton by secondary scattering of the recoiling proton, both in the central and the forward region. The technical solution is further discussed in sections 3.3.2 and 3.5. In addition to the single polarization observables P and T, the combination of recoil polarimetry with the circularly and linearly polarized beams also enables the measurement of the double polarization observables O_x and C_x.

η photoproduction on the *neutron* is presently of particular interest, due to a narrow structure observed in both, excitation function and invariant ηn mass [2, 3, 4, 5]. High neutron detection efficiency and full trigger capability make the BGO ball in combination with the TOF spectrometer particularly well suited for the all-neutral η-n final state. The measurement of single and double polarization observables will be necessary to disentangle the situation. Recoil neutron polarimetry is very challenging, but comes also into range if the ELSA beam intensity will be significantly increased as it is anticipated.[1]

Associated strangeness photoproduction

Due to important physical t-channel background, the role of resonances in associated KY photoproduction is less clear than in non-strange channels. On the other hand, the complete experiment with regard to disentangling the reaction amplitudes comes into reach here. The mandatory recoil polarization measurements do *not* require secondary scattering, due to the self-analyzing weak decay of the hyperons. This counterbalances the small production cross sections. While the Crystal Barrel experiment is presently limited to channels involving K^0_s with subsequent decay into $2\pi^0$, the BGO-OpenDipole setup will in addition provide charged particle ID, including $K^\pm$. It is hence ideally suited to investigate various strangeness channels, also with excited hyperons involved.

The neutron target is of particular interest here again. Contribution of a "missing resonance" $D_{13}(1900)$ was debated since long in the $K^+\Lambda$ channel on the proton [6, 7, 8, 9, 10, 11]. It is expected to show up in $K^0\Lambda$ photoproduction on the neutron as well [12]. This is illustrated in Fig. 2 for the sensitivity to single and double polarization observables.

Despite many recent negative results in search of the much debated Θ^+ antidecuplet state, the latest LEPS result [13] appears to confirm earlier findings of that collaboration in simultaneous K^+K^- photoproduction off a deuteron target. Due to the very similar acceptance to the LEPS experiment, the BGO-OpenDipole setup seems the only place to independently check these results.

Photoproduction of $\Lambda(1405)$

The investigation of the $\Lambda(1405)$ by measuring the t-dependence of the cross section was a goal already addressed in the LoI ELSA/4-03. In the meanwhile it turned out that, as expected, the t-dependence is indeed affected by the production mechanism and the

[1] This is an ongoing research project of the SFB/TR-16.

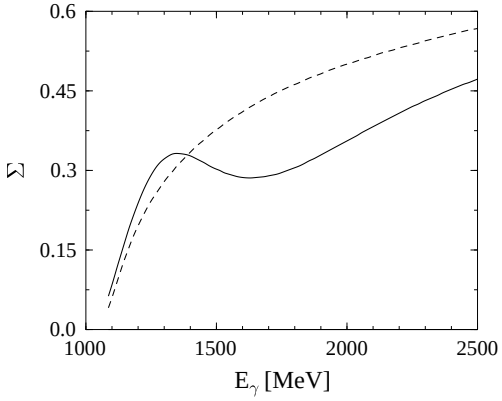

(a) Photon asymmetry Σ with (solid line) and without (broken line) $D_{13}(1900)$ resonance at $\Theta_K^{cm} = 120°$.

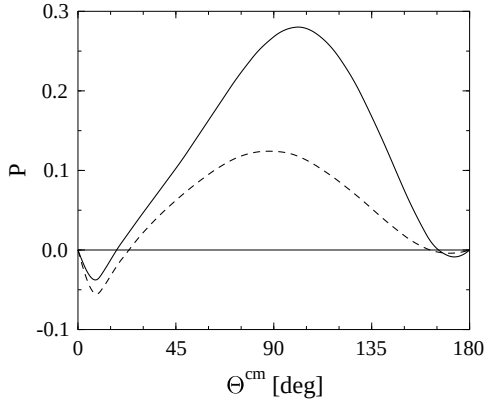

(b) Recoil polarization P with (solid line) and without (broken line) $D_{13}(1900)$ resonance at $W = 1900\,\mathrm{MeV}$.

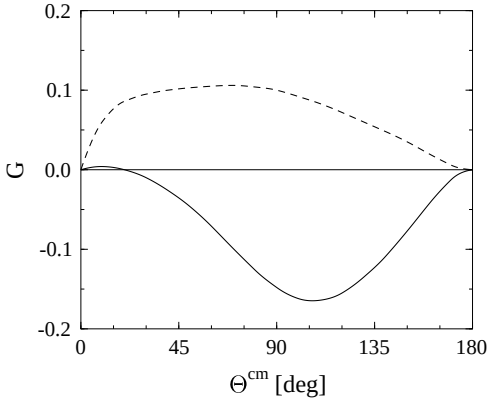

(c) Double polarisation observable G with (solid line) and without (broken line) $D_{13}(1900)$ resonance at $W = 1900\,\mathrm{MeV}$.

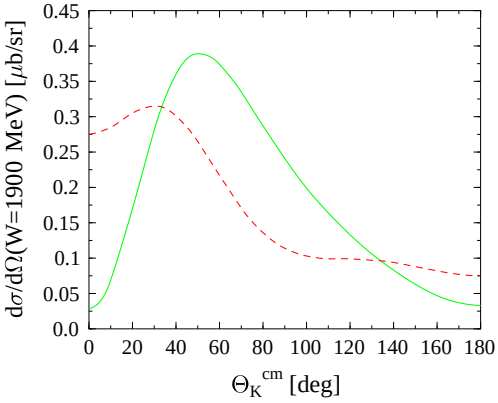

(d) Cross section of the $K^0\,\Lambda$ channel (solid green line) in comparison to $K^+\,\Lambda$ (broken red line) at $W = 1900\,\mathrm{MeV}$.

Figure 2: Kaon-MAID calculation [12] for polarization observables (a–c) and cross section (d) of the $\gamma + n \rightarrow K_s^0\Lambda$ reaction.

possible structure of the $\Lambda(1405)$ [14]. If the so-called double-pole dependence, which is due to initital dissociation of the photon into K^+K^-, was experimentally confirmed, then it would be possible to directly relate the $\Lambda(1405)$ photoproduction to the K^-p scattering length below threshold. This is expected to shed new light on the difficulties of several variants of dynamical coupled-channels calculations to bring the available K^-p scattering data into satisfactory consistency [15] with the recent DEAR results [16] for the strong interaction shift and width of kaonic hydrogen. Moreover, the K^-p interaction which is parameterized in the corresponding scattering length provides the crucial binding force for the formation of a strong molecule-like $\bar{K}N$ component of the total $\Lambda(1405)$ wavefunction.

To uniquely tag the $\Lambda(1405)$ resonance by the $\pi^0\Sigma^0$ decay channel, charged kaon identification is required in combination with hermetic photon acceptance. The reaction is hence well suited to be studied with the BGO-OpenDipole setup.

Photoproduction of vector mesons

The BGO-OpenDipole setup will provide good identification of both charged and neutral pions. Hence, in addition to the $\omega \to \pi^0\gamma$ decay it will be possible to take advantage of the 10 times more abundant $\omega \to \pi^+\pi^-\pi^0$ decay. This will vastly improve statistics in the photoproduction of ω (cf. [17]) and in the $\omega\pi$ channel (cf. [18]). The simultaneous charged/neutral detection capability is of advantage also in the $K^*\Sigma$ (and $K\Sigma^*$) channels with $K^* \to K\pi$ (and $\Sigma^* \to \Lambda/\Sigma\pi$). A recent CB/TAPS experiment to test models of dynamically generated resonances (cf. [19] and references therein) can thus be much improved.

Compared to the case of the ρ, the photoproduction of ω and ϕ mesons is less involved due to the isoscalar nature of ω and ϕ and their small widths of 8.4 and 4.4 MeV. The *ideal* ω-ϕ mixing provides a tool to disentangle different contributions to the mechanism of vector meson production. Since the ϕ is almost entirely $s\bar{s}$, the t-channel exchange of valence quarks and s-channel nucleon resonances are strongly suppressed. ϕ photoproduction provides hence a unique possibility to study the pomeron part of the production mechanism down to small energies. Pomeron exchange is relevant in ω photoproduction, too, but decreasing from higher to lower energy. In threshold vicinity s-channel resonances seem to play a role in ω photoproduction [20, 17] and some of the so far unobserved states of uncorrelated quark models are predicted to have sizeable vector meson-nucleon couplings [21]. Neither in ω nor in ϕ photoproduction the experimental situation presents itself entirely clear, despite recent measurements between threshold and $E_\gamma = 4\,\mathrm{GeV}$ from the CLAS [22, 23], SAPHIR [24] and LEPS [25] collaborations.

The OpenDipole spectrometer is perfectly suited to detect forward ϕ production, i.e. in the small t region. It will thus be possible to clarify the above issues. Using linearly polarised beam will be essential to disentangle natural from unnatural parity exchange. In addition, it will be important to use both proton and deuteron targets, in order to disentangle isoscalar and isovector t-channel exchange. Isospin conservation prohibits π^0 exchange with the isoscalar deuteron in coherent ϕ photoproduction [26, 27, 28].

Medium modification of vector mesons

A special aspect of vector meson production is the study of medium effects of the meson [29, 30]. It is important that the vector meson is implanted practically at rest into the nuclear environment. Momentum balance then requires a forward going recoil nucleon of high momentum. The "magic" photon energy for ω production is $E_\gamma = 2.2\,\mathrm{GeV}$. The BGO-OpenDipole setup is ideally suited to detect the forward going high momentum proton. Over the range of the spectrometer angular acceptance the ω momentum varies by more than the mean nuclear Fermi momentum. For ϕ mesons the magic energy is beyond the ELSA energy range. However, within the range of the nuclear Fermi momentum still magic kinematics can be realized.

3 Present status of the BGO-OpenDipole setup

A schematic of the BGO-OpenDipole detector setup in beamline S of ELSA is shown in Fig. 1 on page 5. Entering from the right, the electron beam produces bremsstrahlung

in front of the tagging system. Various radiator foils can be positioned with a high precision goniometer, in particular a diamond crystal for coherent bremsstrahlung [31]. The photon beam is energy-tagged in the range of approximately 25 – 90 % of the primary beam energy through a vertical bend tagger with 128 overlapping scintillator channels. It hits the target at the center of the BGO Ball. The forward angular region is covered by the Open-Dipole spectrometer instrumented with tracking devices, the aerogel Cherenkov detector and the time-of-flight wall, as briefly outlined in section 1. The status of the individual subdetectors is presented in greater detail in the following.

3.1 Forward spectrometer

3.1.1 Magnet

The central part of the spectrometer is a dipole magnet. Very fortunately, it was possible to get an MD type magnet of practically ideal geometry on permanent loan basis from DESY. The magnet was transported to the experimental area at beamline S (Fig. 3) in April 2007 and was taken into operation for test purposes.

Figure 3: Photo of the magnet after gap extension and ready for the field measurement at the GSI.

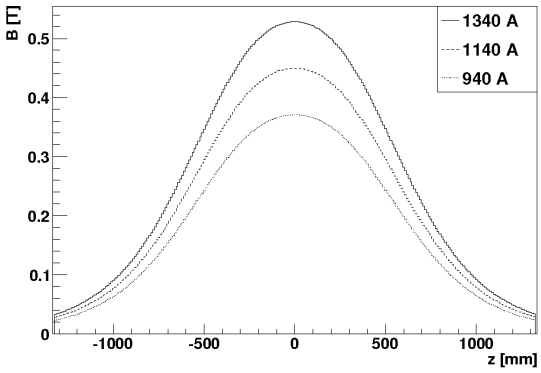

Figure 4: Measured vertical magnetic field along the beam direction with a gap size of 84 cm and currents of 1340, 1140, and 940 A.

The magnet features a variable gap in vertical direction. For largest possible acceptance in forward direction we decided to extend the gap. With an acceptable amount of work and cost it was possible to increase the height from 54 cm to 84 cm. The size of the gap in horizontal dimension is $(W \times D) \approx (1500 \times 1500)$ mm^2. The outer dimensions of the magnet are $(H \times W \times D) \approx (2800 \times 3900 \times 1500)$ mm^3 and the total weight amounts to 90 tons. In March 2009 all modifications of the magnet were completed by an external company. At the foreseen position in the experimental area (2 m distance downstream of the target) an angular acceptance of $\alpha_{hor} \approx 12.1°$ and $\alpha_{ver} \approx 8.2°$ is covered.

With the maximum current $I_{max} = 1340$ A of the available power supply unit at ELSA and the gap height of 84 cm, a central magnetic field strength of $B_{max} = 0.53$ T is achieved (cf. Fig. 4), corresponding to $\int Bdl \approx 0.71$ Tm. This agrees well with simulations. In Fig. 5 the simulated field is shown for $I = 1340$ A coil current and both gap sizes. The simulations have been performed with the CST studio suite 2006. For the 54 cm gap size the result agrees within a few percent with the previous field

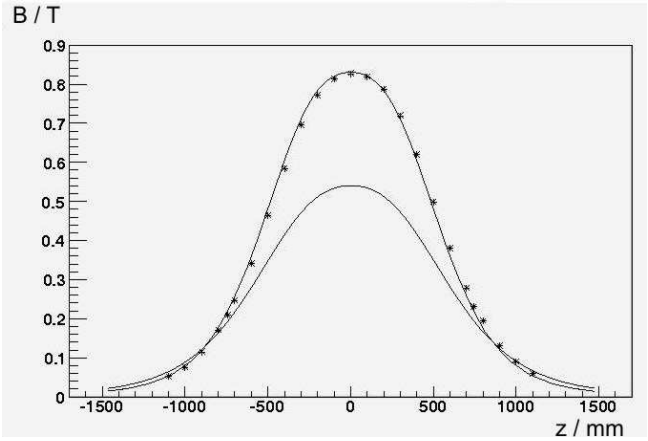

Figure 5: Magnetic field measurement scaled for $I = 1340$ A with vertical gap size of 54 cm. The curves represent simulations for a gap size of 54 cm (upper) and 84 cm (lower). Shown is the vertical field component along the beam line.

measurements at DESY.

Presently a complete field mapping of the dipole magnet with extended gap is performed at the GSI in Darmstadt, using a professional field mapping device which is provided by the magnet technology group. Measurements with variable grid sizes in the range of 10 mm - 50 mm at different currents are scheduled. At each point all three field components (B_x, B_y, B_z) can be simultaneously measured with an accuracy in the order of 10^{-4} T.

It is planned to have the magnet back in Bonn around the middle of the year. Besides rebuilding and connecting, no additional work is required at ELSA. The device will be ready for first testing in fall 2009.

3.1.2 Scintillating fiber detectors

We use two scintillating fiber detectors in front of the magnet, MOMO and SciFi2.

MOMO is a scintillating fiber vertex detector with 672 channels. It consists of three layers of 224 parallel fibers (2.5 mm diameter) each. The layers are rotated by 60° with respect to each other. They are read out through 16-channel Hamamatsu R4760 phototubes (see Fig. 6). The arrangement yields a circularly shaped sensitive detector area of 44 cm diameter. The spatial resolution is about 1.5 mm, yielding effectively more than 50 000 pixels. A 5 cm wide central hole allows the photon beam to pass through.

The detector was originally built for the MOMO experiment at COSY and was successfully used there for the detection of pion and kaon pairs in proton and deuteron induced two meson production reactions [32, 33]. After its transfer from COSY to Bonn, all channels have been tested. A new support structure has been built, fitting to the BGO-OpenDipole setup. The detector is fully equipped and ready for operation.

The **SciFi2** detector was designed and is assembled in the frame of a PhD thesis [34]. It is shown in Fig. 7 (left side). An active area of 66 cm x 51 cm is obtained using 640 scintillating fibers with a diameter of 3 mm. The planar detector covers an angular range of ± 10 deg. in the x-direction and ± 8 deg. in the y-direction. A central hole

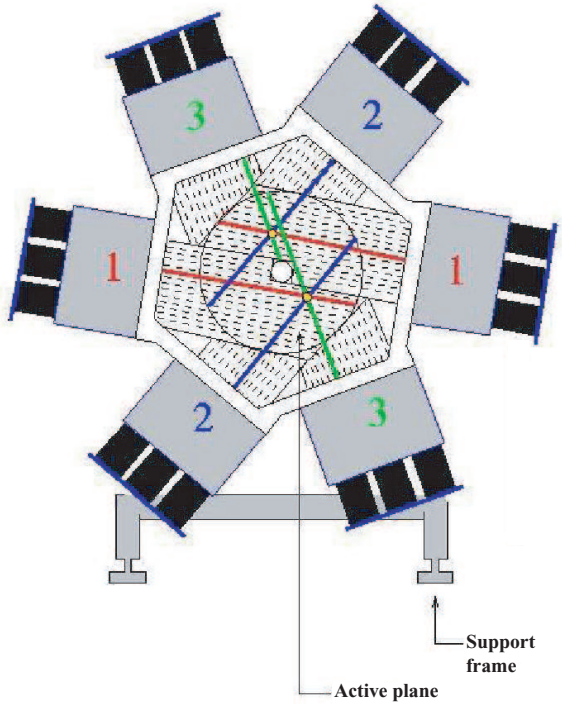

Figure 6: The MOMO scintillating fiber tracking detector

(4 cm x 4 cm) allows the beam to pass through. Groups of 16 fibers are glued together to form so-called modules. The profile of one module is shown in figure 7 (right). The design guarantees a minimum path length (about 2 mm) for particles traversing the circular fibers. The modules are arranged in two layers twisted by 90 degrees. The signals from each module are read out by 16-channel photomultipliers (Hamamatsu H6568).

By now, the modules for one layer are constructed and all components of the frame are ready. All photomultipliers and discriminators have been delivered and tested. The detector will be completed in the early summer of this year.

The analog signals from the phototubes of both detectors are fed to 16-channel leading edge discriminators. The threshold for each channel can be programmed individually via a serial bus. The discriminator outputs then feed multihit TDC modules via a standard LVDS signal format. This signal processing and readout is already successfully used in a very similar way in the Crystal Barrel setup.

The timing resolution of the detectors is about 2 ns (FWHM). It basically results from the varying distance of particle hits to the corresponding photocathode.

3.1.3 Aerogel Cherenkov detector

The aerogel Cherenkov detector (ACD) serves to reliably discriminate pions against protons, and particularly improves the $K^{\pm}$-identification substantially. Results of Monte-Carlo simulations are shown in Figures 8 and 9. They are carried out with realistic relative proton, charged pion and kaon yields within the spectrometer acceptance. For momenta $p < 1300\,\mathrm{MeV/c}$ the number of events is plotted as a function of

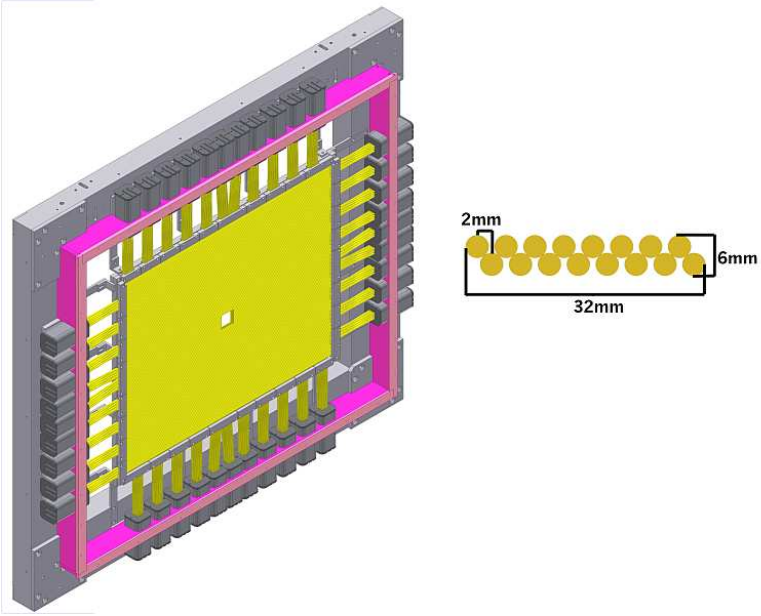

Figure 7: The SciFi2 scintillating fiber tracking detektor

flight-time deviation from kaons, $\Delta t = t_K(p) - t_{\text{measured}}(p)$. Hence $\Delta t = 0$ corresponds to kaons. For lighter particles (pions) which are faster than kaons a positive deviation is obtained, heavier ones (protons) are slower and produce a negative deviation. The upper part of Fig. 9 is for all events using the momentum reconstruction of the spectrometer and the time-of-flight from the TOF detector. The lower part is obtained if a *veto* signal from the ACD is required.

The ACD consists of 5 cm thick aerogel tiles arranged in a wall of 46 x 46 cm^2 front surface within a light collecting box. The inner box surface has a highly diffuse-reflecting paint. The Cherenkov light is detected through 12 photomultipliers. For high efficiency it is crucial that small numbers of Cherenkov photons can be detected. The capability of the photomultipliers to detect single photons was confirmed in tests using white LEDs [35].

Measurements of the efficiency, ϵ_{ACD}, were carried out using electrons behind the (horizontal deflecting) beamline E tagger and with a 1.1 GeV/c pion beam at the HADES cave of the GSI. Both methods yield in very good agreement $\epsilon_{\text{ACD}} = 99.5\,\%$. The result is illustrated in Figure 10 for the pion measurement [36]. In combination with the tagger a good timing resultion of $\tau_{\text{FWHM}} \simeq 6\,\text{ns}$ is achieved (see figure 11).

3.1.4 Drift chambers

Tracking of charged particles behind the spectrometer magnet is performed with eight horizontal drift chambers (DCs) which are built at the PNPI Gatchina. To cover the necessary angular range each DC has a sensitive area of at least 2456 mm $\times$ 1232 mm. The photon beam has to penetrate the DCs. To avoid counting overload by secondary e^+e^- pairs insensitivity spots of 5×5 cm^2 are realized at the center of the chambers by anodizing 6 of the sense wires with gold, thus increasing the total diameter to 100 μm

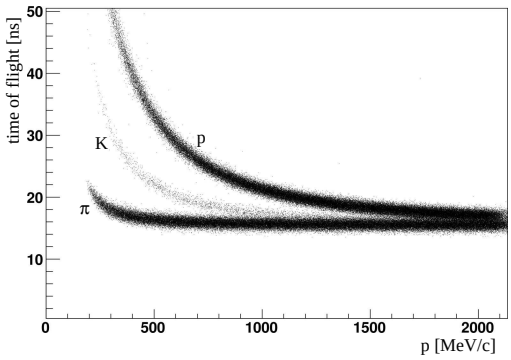

Figure 8: Simulated time–of–flight ($\sigma(\Delta t) = 0.5$ ns) versus reconstructed momentum for pions, kaons and protons.

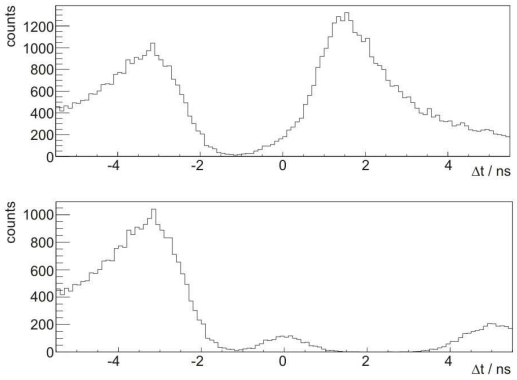

Figure 9: Simulated time–of–flight difference of a particle with $p < 1300$ MeV/c to the calculated time–of–flight of a kaon with the same reconstructed momentum without (top) and with (bottom) a veto signal from the cherenkov counter.

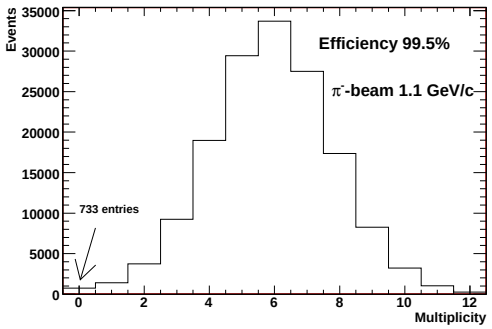

Figure 10: Multplicity of the 12 photomultipliers of the aerogel Cherenkov prototype during the GSI test with 1.1 GeV/c pion beam. From the distribution an efficiency of 99.5 % is deduced.

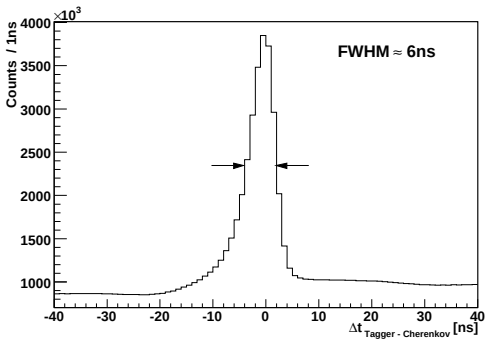

Figure 11: Timing of the aerogel Cherenkov prototype against the tagger during the ω in-medium experiment. A FWHM resolution of 6 ns is achieved.

in the desired area. The effect of this procedure has been successfully tested at PNPI.

The distance of the chambers from the target will range from 3.7 m for the first one to 4.7 m for the last. For accurate positioning and simplified handling the chambers will be suspended from two support bars attached to the magnet. Four of the chambers are rotated by $\pm 9°$ around the beam axis. With two of the remaining chambers having horizontal wires and the other ones vertical wires four different wire orientations are obtained.

The individual chambers have slightly different sizes and wire numbers due to their different orientations (see table 1). The two layer drift cell geometry is identical for all chambers. Figure 12 shows the geometry of the hexagonal drift cells which allows to resolve ambiguities in position reconstruction. To create a nearly symmetric electrical field additional field wires are introduced on both sides of the drift cell layers. The spacing between two anode wires of the same layer is 17 mm.

chamber	angle	sen. area mm^2	width mm	height mm	sen. wires	field wires
X	0°	2456 × 1232	3189	1642	144	436
Y	90°	2456 × 1232	2866	1965	288	868
U	99°	2746 × 1825	3157	2395	304	916
V	81°	2746 × 1825	3157	2395	304	916

Table 1: Sizes and orientations of the four different chamber types

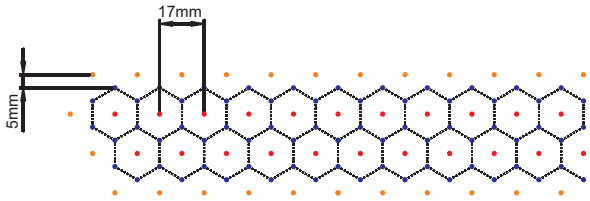

Figure 12: Geometry of the drift cells

The chambers will be operated with a mixture of 70% Argon and 30% CO_2. After mixing the gas will be distributed to each of the chambers individually and vented after passing the chamber. As the flow of 2 l/min in total is small this method was chosen above a more complicated recycling of the gas.

The readout of the chambers is realized with the CROS-3[2] developed by PNPI Gatchina. It consists of four different types of cards:

- CSB – CROS-3 system buffer
- CCB16 – CROS-3 16-channel concentrator board
- CCB10 – CROS-3 10-channel concentrator board
- AD16 – 16-channel amplifier/discriminator card

The AD16 amplifier/discriminator boards are directly attached to the drift chambers. The digitized signals of the frontend boards are send via an LVDS link to the CCB10 concentrators. The CCB10 concentrators transmit their signal to the single CCB16 card. Finally an optical fiber connects the readout system to CSB system buffer implemented as a PCI-card. This cost effective setup minimizes the need for interconnects between the chambers.

To investigate the performance of the chambers and the readout system a prototype chamber was build by PNPI Gatchina and tested within a diploma thesis [37]. During the tests the electronics of the prototype chamber performed without problems up to event rates of several kHz. The position resolution and efficiency could be investigated with high-energetic electrons at the beamline E tagging system. A preliminary drift time relation x(t) was obtained through the drift time spectrum and verified in a separate measurement with a pixel detector. Using this relation the position resolution achieved was well below the design-value of 300 μm.

Results for the chamber efficiency are shown in figure 13. The efficiency is plotted for different high voltages and discriminator thresholds of the electronics. To reduce background two hits in corresponding cells of the two layers have been required. At

[2] **C**oordinate **R**ead**O**ut **S**ystem, third generation

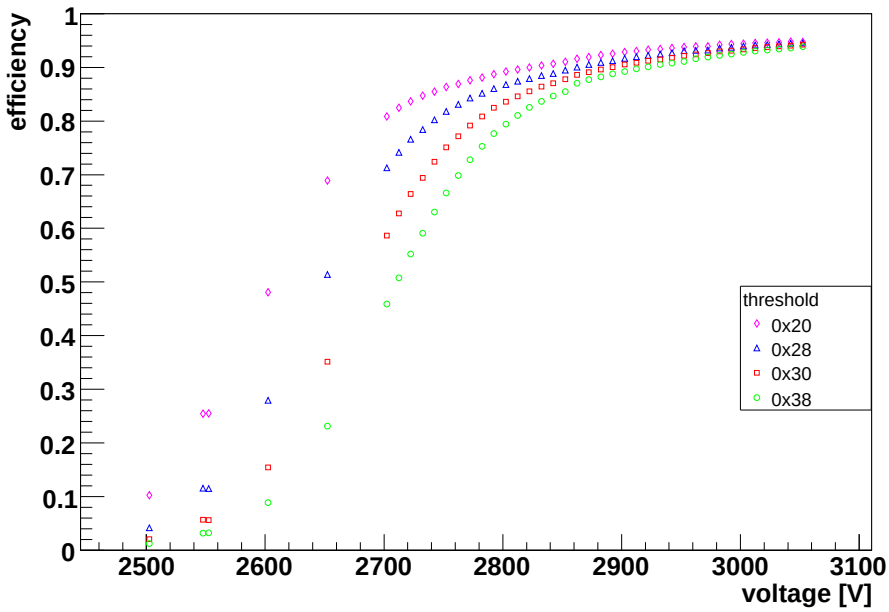

Figure 13: Efficiency of the prototype drift chamber

voltages above 2.9 kV an efficiency plateau of about 94% is reached for all tested thresholds. The efficiency of a single layer of drift cells can be calculated to 97%.

The first two of the full size drift chambers have been delivered to Bonn and are being tested. The two "U" chambers will be ready in May and are scheduled to be delivered together with the remaining chambers in summer this year. The full drift chamber tracking system should be operational by the end of 2009.

3.1.5 TOF detector

The forward spectrometer will be complemented by a time-of-flight (TOF) detector, which is an essential component for particle identification, because it provides flight-time measurements for both, charged particles and neutrons. It has to cover the inner 10–12 degree angular range at a distance of 5 m downstream of the target. An existing detector of the former ELAN experiment is ideally suited for this purpose. It consists of four walls with a 3×3 m^2 front surface, mounted on independent mechanical stands. Each wall houses 14 individual scintillating bars of 3000 mm$\times$200 mm$\times$50 mm size with photomultiplier readout at both ends. This detector has been improved with respect to the light thightness and to the light passage from scintillators to lightguides and photomultipliers. The special discriminators of the former ELAN experiment which, for our purpose, were unfavourably integrated into the aluminium frames of the detector stands are now replaced by external standard electronics. In test measurements using the method described in ref. [38] it was verified that we still achieve a 1-σ resolution in the TDC sum of both bar ends of $\Delta t_{1\sigma} = 0.24$ ns [39], cf. Fig. 14. Measured with cosmics, attenuation lengths of 200–300 cm have been found (see Fig. 15). This is within the expected range for the NE110 scintillating material and hence no ageing is indicated.

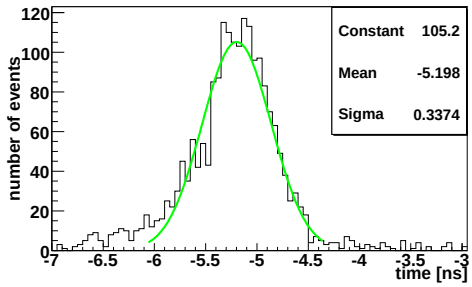

Figure 14: TDC sum resolution of a TOF bar, $\sigma_{TDC-sum} = \sigma_{given}/\sqrt{2} = 0.24ns$

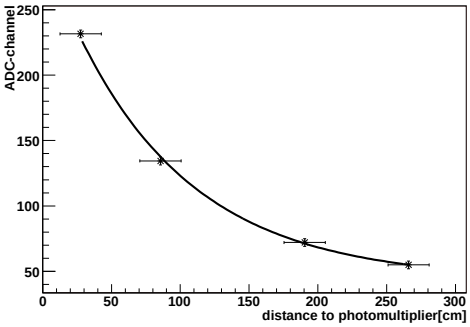

Figure 15: ADC signal of a photomultiplier depending on the distance of the hit to the photomultiplier. The attenuation length of the scintillator is derived by $ADC(x) = ADC_0 \exp \frac{x}{\lambda_{Att}}$

3.2 BGO *Rugby Ball*

The BGO ($Bi_4Ge_3O_{12}$) *Rugby Ball* is a large acceptance calorimeter designed to measure multi-photon states with excellent energy resolution. The design of the calorimeter has taken into consideration a constant thickness in every direction and a central hole of radius 100 mm for the passage of the beam, target and inner detector housing. The resulting structure is made of 480 truncated pyramidal crystals of 240 mm length (corresponding to ~ 21 radiation lengths) arranged in a 15×32 matrix covering the polar angles from 25° to 155° and the whole azimuth for a total solid angle $\Delta\Omega = 11.3$ sr.

The mechanical structure consists of 24 carbon fibre baskets, each containing 20 crystals, and supported by an external steel frame. The baskets are divided into cells to keep the crystals mechanically and optically separated. The thickness of the carbon is 0.38 mm for the inner walls and 0.54 for outer walls. The steel support frame is separable into two moving halves to allow to access the central part of the detector.

The readout of the crystals is performed via photomultiplier tubes directly coupled to the crystals, that allow to obtain an excellent energy resolution also at low energies. Two types of PM tubes are used, depending on the size of the crystals: these are the 2" Hamamatsu R329 and the 1.5" Hamamatsu R580.

3.2.1 Energy trigger.

The *Rugby Ball* can be used to derive fast trigger signals. The present trigger scheme, used at GRAAL, is schematically shown in Fig. 16. The 32 analog signals coming from the crystals positioned at the same polar angle (a crown) enter the C.A.E.N. SY 493 programmable attenuator and delay with adder. The signals are attenuated (0-30dB) and resistively splitted; one half (A) of each signal goes to the adder where the sum of the energy of the crown is performed, while the other half (B) is delayed by 300 ns before being directed to the ADC for processing. The outputs of each of the 15 crown energy sums are eventually summed together to perform the total energy sum of the *Rugby Ball*. This latter analog signal is discriminated and its coincidence with a tagging trigger opens a 800 ns gate for ADC integration.

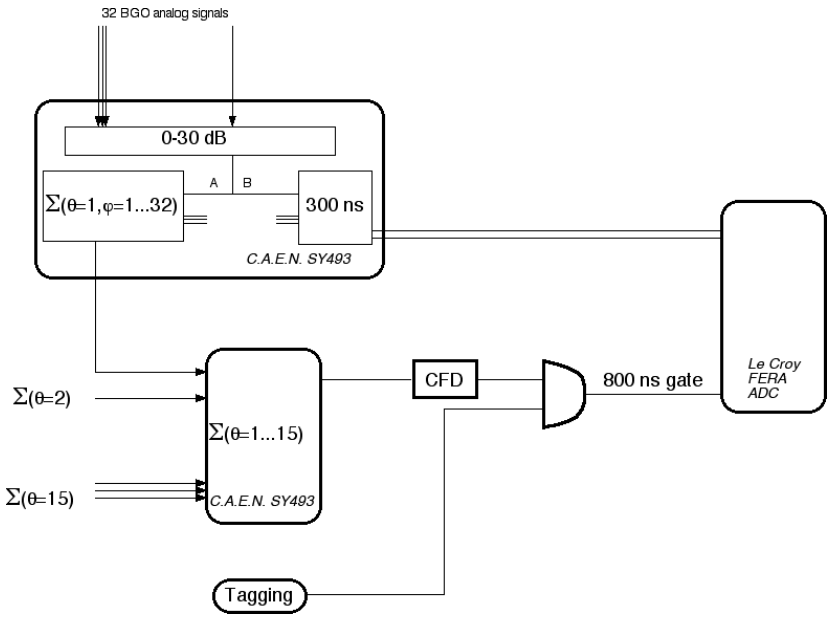

Figure 16: General trigger scheme of the BGO *Rugby Ball*

3.2.2 The *Rugby Ball* as a photon detector.

The BGO calorimeter with photomultiplier readout is optimized for the measurement of multi-photon events. The small radiation length of the BGO allows for a full containment of electromagnetic showers in the 24 cm crystal length, while the value of the BGO Molière radius (2.2 cm) determines a small number of crystals involved in a single shower measurement. A complete report of the performances in photon detection can be found in [40]. Here we recall the more relevant of these performances.

- In Fig. 17 the ratios of the energy collected by the crystal hit by the photon (central crystal) over the total energy collected by the calorimeter (1/tot) and the energy collected by the central crystal + 8 neighboring crystals over the total (9/tot) are displayed. 80% of the energy is collected by the central crystal and more than 95 % by the central + 8 neighboring.
- The cluster multiplicity (number of crystals activated by a shower) is shown in Fig. 18 when a 6 MeV threshold is applied. The multiplicity slowly increases from 4 crystals at low energy to 8 crystals above 1 GeV incident energy.
- The FWHM energy resolution as a function of the incident photon energy is displayed in Fig. 19. The resolution shown is obtained considering the hardware sum of the energy collected by the crystals, the software sum being slightly worse and depending on the applied threshold. The resolution is already excellent at low energy ($\sim 6\%$) and reaches the 3% level at 1 GeV.
- Finally the behavior of the resolution (at the given photon energy) as a function of the event rate is shown in Fig. 20. We can see that there is no substantial worsening of the resolution at rates up to 2 kHz. At higher rates (3 kHz and above) the resolution is worsened by a factor ~ 2.

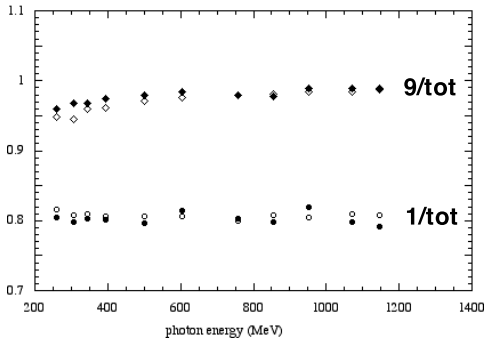

Figure 17: Ratios of the energy collected by the central crystal (1/tot) and on the central plus the 8 neighboring crystals (9/tot) over the total energy. Full points: experiment, open points: montecarlo

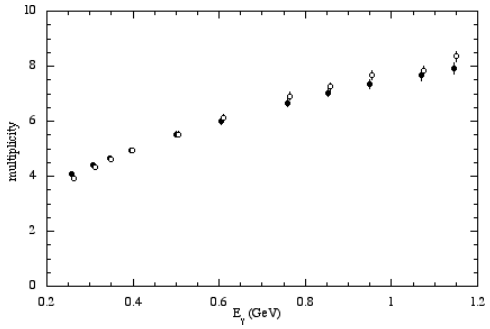

Figure 18: Event multiplicity (i.e. number of crystals collecting more than 6 MeV) as a function of the incident photon energy. Full points: experiment, open points: montecarlo

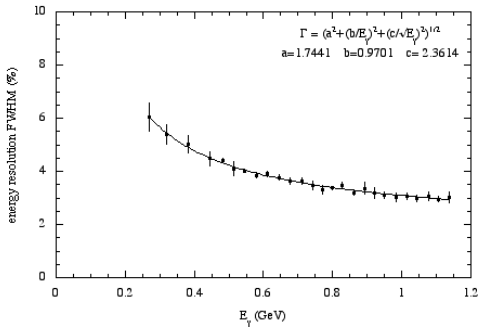

Figure 19: FWHM energy resolution of the hardware sum of the analog signals.

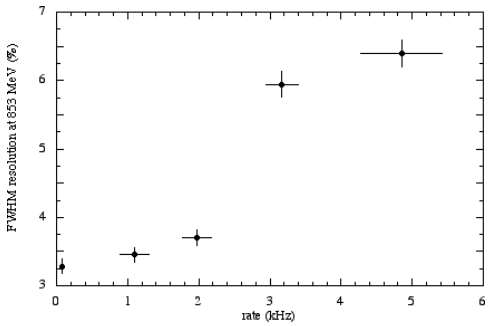

Figure 20: FWHM energy resolution for a 853 MeV photon as a function of the event rate.

3.2.3 Multi-photon detection

The *Rugby Ball* has operated at GRAAL photon beam for almost ten years, showing its capability in the detection of multi particle final states with more than one photon. The detection of π^0 and η mesons is unambiguous: peaks are clearly separated even in the raw data. In Fig. 21 we show the two photon invariant mass distribution obtained with a Hydrogen target measurement in three different conditions: upper curve (black) is the distribution without any condition; mid curve (red) is the same distribution with the requirement of the detection of a charged particle in the apparatus in coincidence with the two photons in the BGO and lower curve (blue) is obtained by requiring the charged particle to be a proton and the kinematics to be fulfilled. The displayed values of π^0 and η masses and widths refer to this last distribution. We can see that the remaining background under the meson peak is $\sim 0.4\%$ for the π^0 peak and $\sim 1\%$ for the η peak. The six photon invariant mass distribution, corresponding to the decay $\eta \to 3\pi^0 \to 6\gamma$ is shown in Fig. 22, with the same color code. The η signal is still very clear even though the signal/background is slightly worse as are the mass value and width.

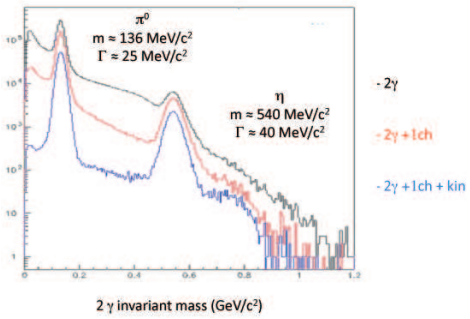

Figure 21: Two-photon invariant mass distribution obtained at GRAAL. Black (upper) curve: two photons in BGO; red (mid) curve: two photons in BGO and a charged particle in the apparatus; blue (lower curve): two photons in BGO and a charged particle in the apparatus fulfilling the kinematics

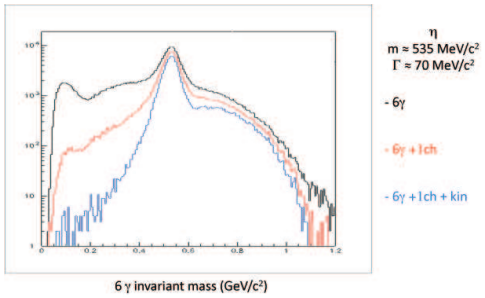

Figure 22: Six-photon invariant mass distribution obtained at GRAAL. Black (upper) curve: six photons in BGO; red (mid) curve: six photons in BGO and a charged particle in the apparatus; blue (lower curve): six photons in BGO and a charged particle in the apparatus fulfilling the kinematics

3.2.4 Charged particles

The *Rugby Ball* is sensitive to all charged particles. In most cases, only the particle position can be obtained but not its energy. This is always true for charged pions and charged kaons. On the other hand electrons and positrons are measured with the same performances as for the photons. For low energy protons the energy can be measured with a good accuracy [41]. The typical spectrum of a monoenergetic proton impinging on the BGO shows an ionization peak with a low energy tail caused by nuclear interactions. The tail to peak ratio increases as a function of the proton kinetic energy T_p (Fig. 23). When T_p is greater than 300 MeV, the proton escapes from the detector. Other characteristics of the BGO as a detector of charged particles (pions, deuterons) can be found in [42].

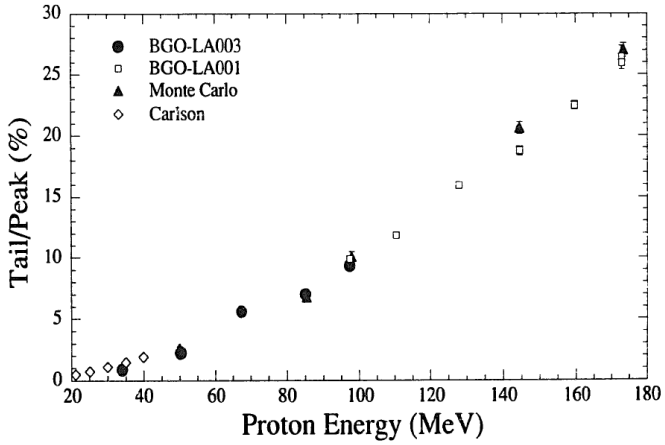

Figure 23: Tail to peak ratio of the response of one BGO crystal to protons as a function of the proton kinetic energy

3.2.5 Neutrons

The BGO is sensitive to neutrons via various neutron induced reactions on Oxygen, Germanium and Bismuth. The efficiency for neutron detection is high, up to $\sim 60\%$, but strongly depends on the threshold value applied [1]. For absolute cross-section measurements this requires special attention, but it is much less critical for asymmetries. The good neutron detection efficiency in combination with its full trigger capability makes the BGO Ball certainly well suited for quasifree n measurements using deuterium target and detecting the recoil neutrons.

3.2.6 Calibration and monitoring

The absolute calibration of crystals is obtained using the 1.27 MeV photons from 3 to 6 ^{22}Na sources placed around the target vacuum tube. The response of the 480 BGO sectors is equalized using an automatic procedure, that sets all the PM's gains by varying their high voltage. An attenuation factor is eventually introduced at the SY 493 level to allow for data taking in beam conditions. At GRAAL the calibration constants used were $\simeq 0.02$ MeV/channel allowing to measure $\simeq 1.15$ GeV of energy in a single crystal. The experimental conditions at ELSA should not be very different.

The calibration constants of each crystal may vary as a function of time, due to two main reasons: variations of the crystal light output due to temperature effects and variations of the PM gain. A full description of the method adopted at GRAAL to monitor the PM stability is given in [43], while the temperature monitoring system is described in details in [44].

3.2.7 Scintillator barrel

The BGO calorimeter is coupled to a scintillator barrel to distinguish charged vs. neutral electromagnetic showers and to identify protons and pions, when possible, via ΔE/E measurement. The barrel is composed of 32 plastic scintillators (same azimuth modularity of the calorimeter) of $\simeq 430$ mm length and 5 mm thickness housed in a carbon fiber support, that separates the counters optically and mechanically. Each scintillator is coupled to a Hamamatsu R1635 photomultiplier (linearity selected) through a light guide. The barrel can be used also as a charged multiplicity trigger. In the free space between the target and the barrel, extra detectors can be housed, e.g. cylindrical wire chambers for tracking.

3.3 Further detector components

3.3.1 Central Tracker

The tracks of charged particles emitted within the angular and momentum acceptance of the BGO Ball will be reconstructed from the coordinates of point of intersections of the tracks with two coaxial cylindrical multiwire proportional chambers (MWPCs) with cathode strip readout. These MWPCs will be very similar to the ones previously used by the GRAAL collaboration in Grenoble [45] and by the GDH collaboration in Mainz [46]. They will be built by the group from INFN -Pavia which has recently built a similar set-up for the CB@MAMI collaboration. A schematic view of a MWPC is depicted in Fig. 24.

The inner and the outer walls are made from 2 mm thick Rohacell (a polymethacrilate foam having a density of 0.05 g/cm^3) covered by a 20μm kapton film. Both interior surfaces are laminated with copper strips, 0.02 μm, 4 mm wide and separated by 0.5 mm wide gaps. The strip will be covered by a 0.01 μm tin layer in order to have a stable long-term conductivity. These cathode strips are wound helically in opposite directions at angles of $\pm 45^\circ$ with respect to the axis of the cylinder.

The anode consists of arrays of 20 μm diameter tungsten wires stretched parallel to the cylinder axis, separated from both cathode planes by 4 mm gaps. The wires are separated in 2 mm intervals around the circumference of the chamber and maintained at a tension of 60 g.

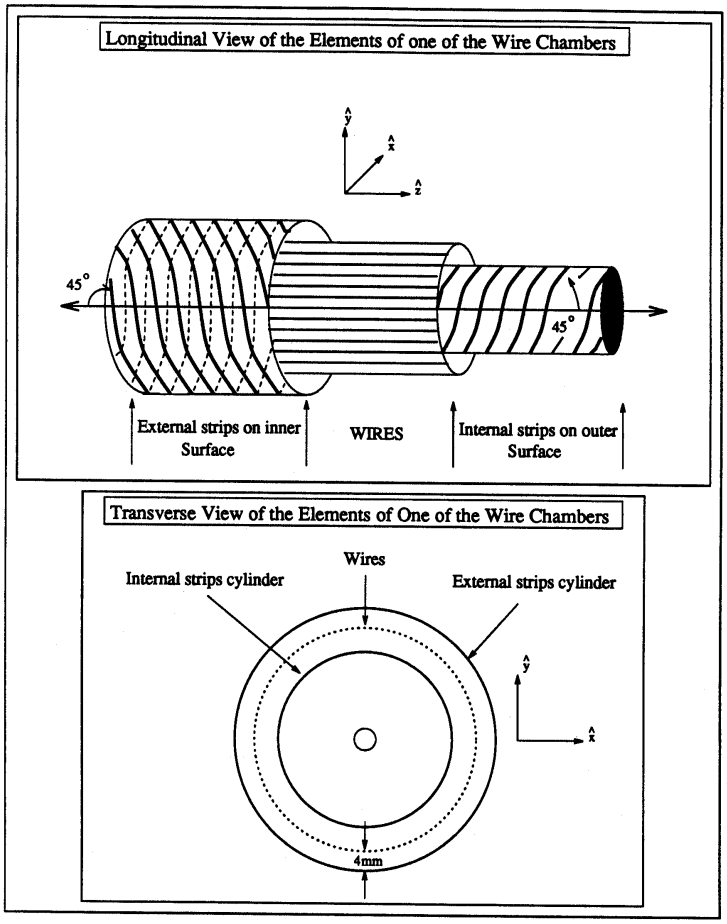

Figure 24: Schematic view of a multiwire proportional chamber

The preliminary geometrical characteristics of each chamber are reported in table 2.

A mixture of argon(79.5%), ethane (30%) and freon-CF_4 (0.5%) will be used as the filling gas. This mixture is a compromise between charge multiplication and localization requirements imposed by the ionizing particle tracks.

Within each chamber both the azimuthal and the longitudinal coordinates of the avalanche will be evaluated from the centroid of the charge distribution induced on the cathode strips. The location of the hit wires(s) will be used to resolve ambiguities which arise from the fact that each pair of inner and outer strip crosses each other

Table 2: Preliminary geometrical characteristics of the MWPCs

	Chamber 1	Chamber 2
Length (mm)	400	500
wire plane diameter (mm)	104	164
Number of wires	160	256
Inner cathode diameter (mm)	96	112
Number of internal strips	48	56
Outer cathode diameter (mm)	160	176
Number of external strips	80	88

twice. The expected angular resolution (rms) will be $\approx 1^\circ$ in the polar emission angle ϑ and $\approx 2^\circ$ in the azimuthal emission angle φ.

The read-out electronics for the central tracker will be built by the INR-Moscow group and will be based on the ITEP developments for the EPECUR experiment [47]. MWPC anode wire signals are treated by the so-called "wire proportional chamber board" (WPCB). Each WPCB contains 100 identical analog channels, Xilinx FPGA chip, Cypress USB microprocessor, discriminator level DAC and power conditioning components. A WPCB block diagram is shown in fig. 25.

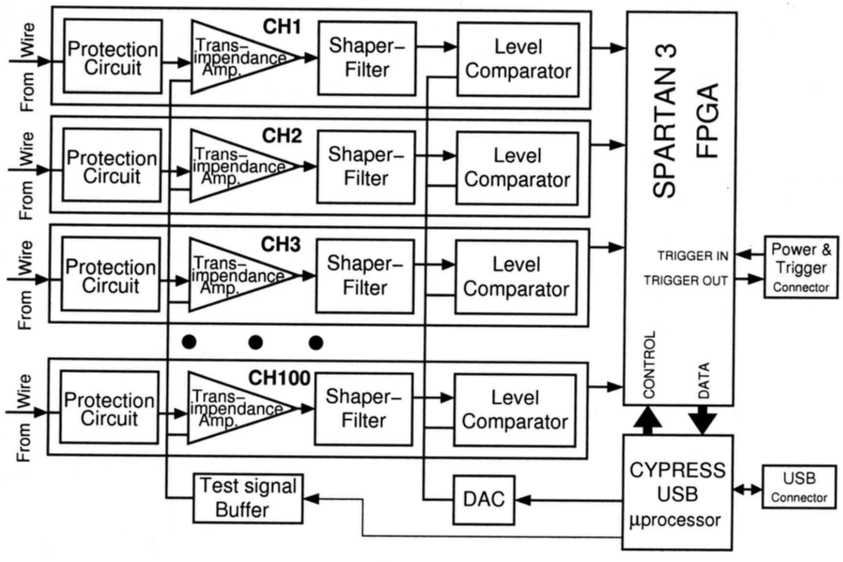

Figure 1. Proportional chamber board block diagram.

Figure 25: Schematic bloc diagram of the WPCB.

The input of each channel is resistively connected to the ground to provide zero potential to the signal wire. The diode-based low capacitance protection circuit prevents the input from over-voltage in case of spark discharge in the chamber. The fast current

sensitive transimpendance amplifier is based on a 1.2 GHz 1C chip and provides the signal amplification of 5 mV/μA. The RC shaper-filter is designed to cut out the long tail of the charge collection signal and to reduce the high frequency noise component on the amplifier output. A fast comparator with TTL output is used to form the leading edge discriminator. All channels have common discrimination threshold programmable in 1 mV steps by means of a serial DAC controlled by the microprocessor. The amplitude spread of the signals at the comparator input is in the range of 10 mV to 50 mV. Rather low amplification allows to avoid oscillation problems and makes the amplifier stage cost effective. At the same time a careful choice of the comparator with low offset voltage of several mV is necessary.

A WPCB sample is currently under test by the INR. The preliminary analysis of the available sample and the positive experience of operation at EPECUR show that it is suitable for the BGO-OpenDipole experiment and that only small modifications will be needed.

Signals from MWPC strips will be treated by the "strip proportional chamber boards" (SPCB), still under developement. They will contain about 100 identical channel preamplifiers mounted on the edge of the MWPC. Its layout will be similar but simpler than the one of the WPCBs, since the discrimination part is not needed in this case. A sample for the SPCBs will be ordered and tested at the INR test laboratory.

3.3.2 Si vertex detector

Silicon sensors facilitate the construction of very compact detector arrays for charged particles with very high position resolution and efficiency at moderate cost in terms of material budget. Sensors can be produced in different shapes with thicknesses of less than 300 μm routinely achieved for a two-dimensional spatial resolution below 10 μm. Radiation-hard designs allow operation up to integrated fluences of more than $10^{15}\,\mathrm{cm}^{-2}$.

Readout of silicon detectors is fast. The readout electronics has to be mounted in the vicinity of the detectors to avoid creation of noise caused by cable capacitances.

Because of their properties, in particular the excellent spatial resolution and fast signal as well as high efficiency, Si sensors are particularly well suited for measurements such as the detection of tracks of particles originating from secondary decay vertices, e.g. the decay of hyperons, in particular Λ baryons and mesons such as the $\mathrm{K}_S \rightarrow \pi^+\pi^-$ decay. Decay lengths of several cm (e.g. $c\tau = 7.8\,\mathrm{cm}$ for the Λ) then allow identification of long-lived particles and reconstruction of their four-momentum from the event topology. Therefore, a setup featuring several layers of Si sensors close to the target will help in the identification of strange particles, either by direct reconstruction of decay Vees or by identification of decay kinks which are indicative of the secondary decay of charged hyperons, e.g. $\Sigma^+ \rightarrow n\pi^+$ or $p\pi^0$.

The setup includes a Si tracker layer in forward direction with a square shape constructed from large double-sided rectangular sensors. This layer will primarily serve to close the gap in tracking betweeen the acceptance of the magnetic spectrometer and that of the Central Tracker (CT). It may also serve to provide a first track point close to the target for particles entering the acceptance of the spectrometer. A single track point outside of the magnetic field region close to the target, measured with good time

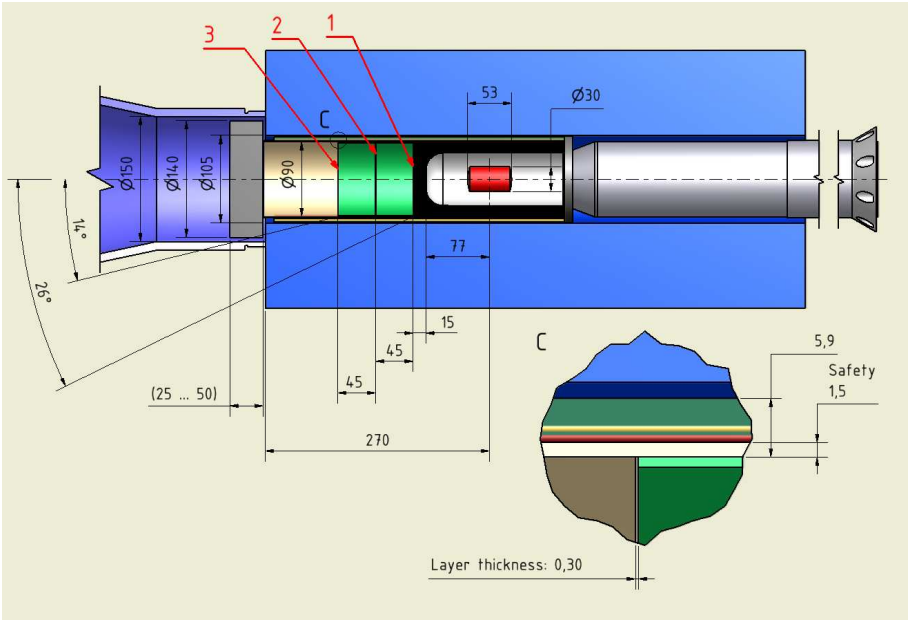

Figure 26: Schematics of the configuration of Si-vertex detectors and carbon analyser inside the BGO ball. The Si layers are labelled 1-3, C is the Central Tracker. In this view beam direction is from right to left. The optional carbon analyser (grey) for polarization measurements is placed at the exit of the CT (see also section 3.5).

resolution, greatly aids in the track reconstruction, since it can be used as a seed for primary tracks as well as secondary ones.

Additional tracking layers will make use of circular double-sided silicon strip sensors inside the CT, cf. Fig. 26. These strip detectors can possibly have diameters of up to 9 cm. A first layer will be placed as close as possible to the target to provide a first tracking point for secondary decays very close to the decay point. Several consecutive layers will define particle trajectories with very good resolution. This arrangement is also suited for polarization measurements of protons using secondary scattering in a slab of carbon (see Fig. 26). After scattering, protons are further tracked in the square shape detector layer. Polarimetry is further discussed in section 3.5.

First test measurements with small detectors have been performed. The sensors have an area of 2×2 cm^2 and pitches of 50 μm on both, x and y side. Source tests with Sr-90 β decay electrons as well as using electrons in setups behind the beamline E tagger exhibit very good spatial resolutions. Radiation hardness has been studied in experiments with neutron sources, nuclear reactor neutrons and, most recently, during tests at the photon beam behind the Crystal Barrel setup. The sensors produced in non-radiation-hard design were kept in the direct photon beam for several days without significant loss in performance and only slight increase in reverse current. Quantitative analysis is underway. The test measurements show, however, that radiation-hard sensors can be operated close to the target of photoproduction experiments without leaving holes for the beam to pass through. This greatly increases the accessible solid angle in particular for small polar angles.

The full data acquisition chain for sensors equipped with APV25 S1 asics (originally used in the CMS experiment at the LHC) is available. The test sensors are mounted

in a fashion that allows irradiation of the sensors so that the particles do not traverse any structural elements. This is important also in the very compact mounting scheme foreseen for the sensors inside the MWPC. The current setup employing APVs as front-ends can only be read out using external triggers. These will have to be provided by the other detector components of the setup.

3.4 Tagger

The tagging magnet which previously had been employed for Crystal-Barrel/TAPS and SAPHIR at beamline S of ELSA will be used again for the BGO-OpenDipole setup. A new focal plane instrumentation will be installed consisting of 128 overlapping scintillators, which provides a resolution in photon energy of 10 – 50 MeV (energy dependent, full bin width). This is about a factor 3 worse compared to the scintillating fiber detector of beamline E, but still sufficient for many reactions with low cross section, e.g. kaon or ϕ production, where relatively large binning in E_γ is acceptable due to the small yields. To explore the option of an additional scintillating fiber detector with Silicon Photomultiplier readout, a prototype is presently built at the University of Moscow.

The focal plane instrumentation will be held compatible with the design of a new detector ladder of the beamline E tagger. Modularity ensures that, if required, parts can be easily exchanged among the two taggers.

The coincidence conditions and the derivation of the trigger signal from the tagger will be done in FPGA modules. Those also allow the integration of a scaler to count the signals channel by channel, even with a digital delay to apply a dead time gate to the scaler values. The FPGA modules are presently under development and test.

The photon beamline starts at the tagger magnet and extends into the BGO Ball where it is part of the target system. It will contain collimators with apertures of 4 – 10 mm, such that the degree of linear polarization is increased. The charged debris of the collimation will then be removed by a small cleaning magnet and a second collimator with slightly larger aperture.

Various bremsstrahlung radiators can be positioned in the electron beam. A goniometer serves for the exact alignment of the diamond crystal for coherent bremsstrahlung [31]. The goniometer has been tested in the laboratory to ensure absolute position and repetition stability. It is ready for operation.

At present, the tagger is instrumented with scintillators from the former SAPHIR experiment. This enables immediate beam tests with modest energy resolution already before the new focal plane instrumentation will be available.

3.5 Options for polarimetry

Polarisation measurements of nucleons are achieved through scattering off nuclei. The scattered nucleon exhibits an azimuthal angular modulation related to its transverse polarisation components :

$$N\left(\phi_{sc}\right) = N_0[1 + A(T_p, \theta_{sc})(P_y cos(\phi_{sc}) - P_x cos(\phi_{sc}))] \quad (1)$$

where θ_{sc} and ϕ_{sc} are the scattered angles of the nucleon and $A(T_p, \theta_{sc})$ is the analysing power, characteristic of the scattering reaction. Many measurements of the

proton analysing power on Carbon have been made for proton energies up to 1 GeV, which are typical for recoil protons in meson production at ELSA. In principle by inserting a sufficient thickness of graphite into the detector systems, for the recoiling nucleons to scatter in, this technique can be used to determine the recoil nucleon polarisation.
Measurement of recoil polarisation will require knowledge of,

1. The final state reaction channel
2. The initial recoil nucleon momentum
3. The direction of the secondary scattered nucleon
4. The analysing power

Item 1 requires the near 4π detection of charged and neutral mesons, which will be provided by the BGO-OpenDipole detector systems.
Item 2 can be achieved in two ways, either direct measurement with a tracking system or, given complete knowledge of the final state meson, through a kinematic reconstruction. This second method would be particularly appropriate for neutral meson detection in the BGO ball e.g. π^0, η.
Item 3 must be measured directly through subsequent detection after the graphite scatterer. For protons recoiling at angles backwards of 25° this would be achieved by exploiting the planned central tracking system, by positioning a cylinder of graphite between the target and Central Tracker. In forward direction the proton direction can be accurately determined using the Si-vertex detector described in section 3.3.2. A possible arrangement is depicted in Fig. 26 on page 25. After secondary scattering in the carbon plate, the outgoing protons will be tracked in the square shaped Si layers discussed in 3.3.2, and in the forward spectrometer.

Placing a wall of graphite alternatively between the Drift Chambers may add the possibility in the forward region to precess the spin of the proton in the dipole magnet. This precession would give access to the z component of polarisation and two additional observables O_z and C_z.
Item 4 can be determined via a Monte Carlo integration of the proton-Carbon analysing power through the detector acceptance.

A similar technique has been developed with the CrystalBall at MAMI, where 2cm of graphite enabled a scattering efficiency of approximately 3% for recoil protons with an analysing power of around 0.2. A similar figure of merit should be achievable with the BGO-OpenDipole setup.

3.6 Liquid hydrogen and deuterium target

The target cell and the cryogenic system will be located directly behind the beam dump along the beam direction. The cell is contained in a vacuum pipe, which guarantees the thermal insulation, and it is surrounded hermetically by the BGO Ball.

The target cell (see fig. 27 and 28(a)) is a 4 cm diameter aluminum cylinder, closed by thin mylar windows at the two sides. Two different lengths of the cell are available (6 and 11 cm) in order to fulfill different experimental requirements. The target cell can be filled either with liquid Hydrogen (H_2) or Deuterium (D_2).

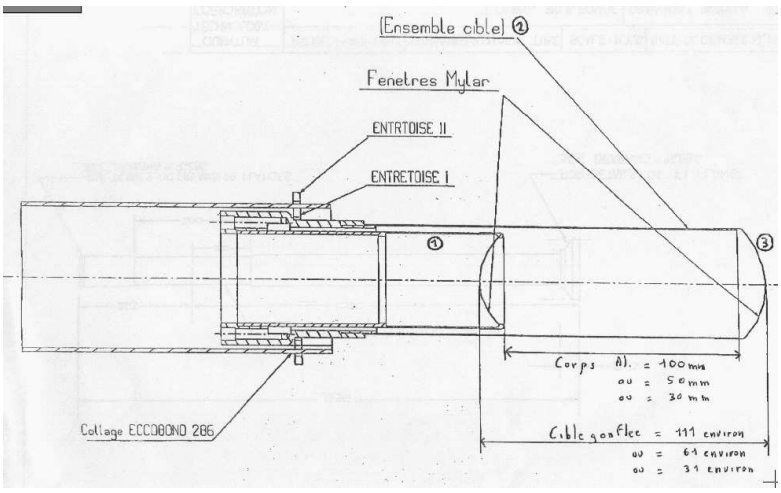

Figure 27: Schematics of the target cell.

The cryogenerator is compromises: a) a helium compressor (with a 100 l external helium buffer tank); b) a two-stages cold head (working at the nominal temperatures of 70K and 20K); c) a cryostat (Quantum Technology Corp.). The cryostat (see fig. 28(b)) is a closed-cycle refrigerator, working with high purity helium gas: inside the cryostat the temperature of the refrigerating helium is cooled down via two Gifford-McMahon (G-M) cycles with helium gas pressure cycled isothermally from 17 bar relative (250 psig) to 5 bar relative (70 psig). The hydrogen/deuterium gas is cooled down by the helium through heat exchangers and liquefied inside the cell.

The target temperature is constantly monitored by three probes and stabilized by a heating resistor. One of the probes is connected with a safety system which automatically stops the compressor in order to avoid freezing of the liquid inside the cell.

When the cell is filled up, the working temperature of the liquid Hydrogen or Deuterium is about 17K and 22K, respectively.

The hydrogen and deuterium gas is stored in two tanks (454 l), connected in parallel to the same distribution panel, so that the change from Hydrogen to Deuterium target (or vice-versa) can be made by simply switching from one tank to another, after a purge and pump procedure.

The alignement of the target with respect to the beam will be provided by a regulation system, with displacements and tilts both in the vertical and horizontal directions. The frame containing the target pipe and the cryostat will move on rails for the extraction of the whole system along a direction perpendicular to the beam.

A remote control system will allow the constant monitoring of the target temperatures and pressure.

In figure 29, the configuration of the target and the cryostat in the experimental area is shown.

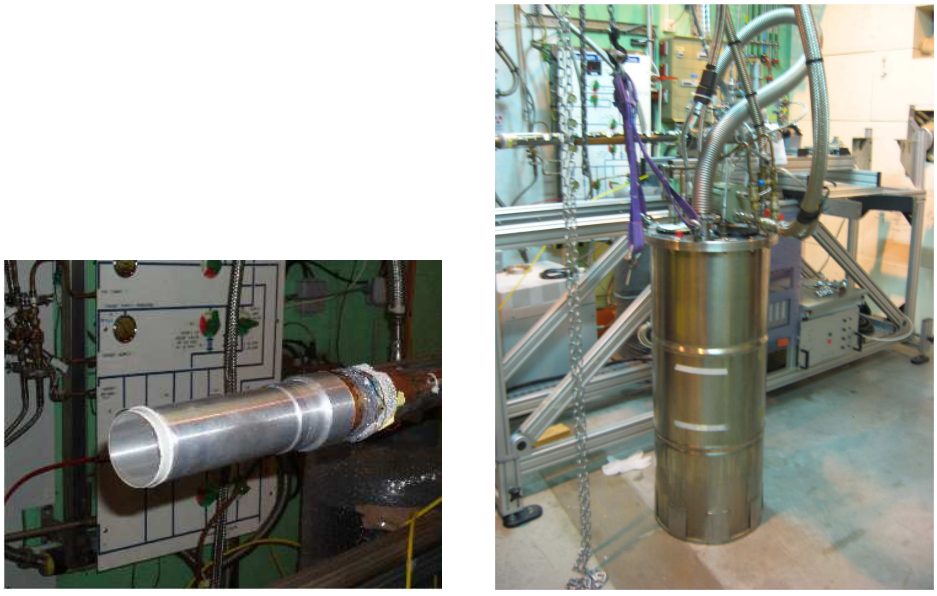

(a) Target (b) Cryostat

Figure 28: Panel (a) shows the external part of the target cell. Panel (b) shows the cryostat used to liquefy the Deuterium (or Hydrogen) inside the cell.

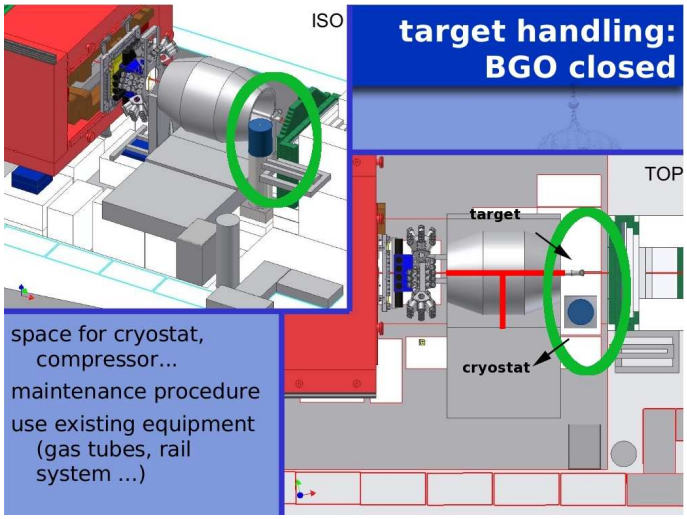

Figure 29: Position of target and cryostat at beamline S

4 Commissioning of the detector system

The detector system will be set up in several steps. The basic first one is the installation of the spectrometer dipole magnet. It is presently at the GSI, Darmstadt, for field mapping which is planned to be finished in July. After reinstallation at the S-area the setup of the detectors will begin.

Each individual detector subsystem has its own mounting frame. The frames are aligned relative to the beam axis and the spectrometer dipole. The magnet itself provides the basis for the drift chamber mounts, which will hold the chambers from above, as can be seen from Fig.1 (overall setup) on page 9. Directly upon finishing the installations, the subdetectors will be taken into operation and tests of readout and basic functionality will be performed. For parts of this testing (untagged) photon beam will be useful. Several short beamtimes no longer than 1 – 2 days will be required on short term basis. The setup and testing is outlined in more detail in the following.

The first subdetector to be taken into operation at the experimental area is the x-tracker of the DC package, which is presently under high voltage and cosmics test in the laboratory. The rest of the DC package is scheduled to be delivered in summer and then first has to undergo laboratory tests. By that time the scintillating fiber detectors MOMO and SciFi2 shall be installed and ready for on-site tests. After this, the aerogel Cherenkov detector will be installed. It is fully tested and had already been used in recent Crystal-Barrel experiments. In the meanwhile, the remaining DC tracker packages shall be ready for installation in the area. Finally, the TOF walls will conclude the detector installations. A new dedicated readout and data acquisition system is presently set up, which is based on the Crystal Barrel system.

After basic functionality tests of the individual subdetectors, the first goal of the commissioning of the spectrometer will be the track finding within the front tracker (MOMO-SciFi2), FT, and back tracker (DCs), BT, using protons photoproduced by an untagged beam from a simple solid target, e.g. CH_2. The next step is then the track finding and reconstruction between FT and BT, still without magnetic field. A carbon scatterer inside the magnet gap may be used to test the reconstruction with a deflection between FT and BT. The major step will then be the tracking of protons and other charged particles through the magnetic dipole field and, finally, particle ID using the momentum measured by the spectrometer and the flight time measured by the TOF scintillator wall. Enhanced by the aerogel Cherenkov detector, the goal is then to achieve a clean, simultaneous $K^{\pm}$ identification. This is expected from simulations as is illustrated in Fig. 9 (see page 14).

After the spectrometer magnet is in position, also the BGO calorimeter (the mechanical structure, the crystals and the cables) will be installed at the S-beamline, partly in parallel with the installation of the FT and BT devices. The different geometrical conditions of the S-beamline compared to GRAAL require a new larger platform for the detector, which allows the full opening of the two halves of the sphere on both sides of the beam-pipe for a convenient access to the inner detectors, to the target and to the MOMO detector.

A removable roof above the calorimeter and a tent around it will minimize daily temperature variations in the region of the detector.

In a first step (end 2009-mid 2010), we will maintain the BGO electronic read-out system used at GRAAL, based on 32 Lecroy 4300B FERA ADC modules (CAMAC

standard), for the analog-to-digital conversion of the signals produced by the release of energy inside the crystals. They will be piloted by a new VMIVME-7807 RC processor (VME standard) in order to provide full compatibility with the general acquisition system.

In a second step (end of 2010), the electronics will be replaced by 32 Wiener AVM16 Sampling ADC modules, which will provide information on the start time of the signal, therefore allowing the off-line rejection of time-uncorrelated random events.

The second part of 2009 and the first part of 2010 will be devoted to the tests of the crystals' and PMs' response and to the setting-up of the calibration and monitoring procedures.

The response of the crystals to a ^{22}Na source will be equalized with an automatic procedure which sets the photomultiplier high voltages in order to center this response around the same ADC channel for all crystals. Possible drifts in photomultiplier gain can be corrected *a posteriori* by acquiring the response to the ^{22}Na source at least twice per day and using, during the analysis, the exact values of the calibration constants. This will also allow to account for possible day-night temperature fluctuations of the crystals, which are responsible for small changes in the BGO light yield.

Signals produced by a particle in the crystal are attenuated inside the mixers (as already explained in section 3.2.1), before being processed by the ADC modules, and this allows to expand the ADC dynamical range from few hundreds of keV up to 1-2 GeV. The extrapolation of the calibration constants from the MeV-region of the gamma source to the GeV-region of the maximum energy deposited in a single crystal requires that possible non-linear behaviours of the electronics chain (PMs, Mixer and FERA ADC) are kept under control and corrected off-line.

The linearity curves will be obtained, at the beginning of each data taking period, from the comparison of the response of the BGO read-out chain and of a reference NaI detector to the light of LEDs, which can be varied in intensity and which simulate the signal produced by particles with energies ranging from few MeV up to 2 GeV. These curves will allow to correct the calibration of each crystal as a function of the ADC channel.

The monitoring of the calibration of the crystals will allow to reduce and/or correct *a posteriori* the sources that affect the energy resolution of the calorimeter, in order to keep this resolution around 3% (FWHM) at 1 GeV, as it was measured during the beam tests ([40]).

The first experimental tests which will allow to check the correct working of the calibration and monitoring procedures will be the off-line reconstruction of the 2-photon invariant mass, in coincidence with the detection of a proton in the apparatus. From the spectrum, as already explained in section 3.2.3, a clear separation of the π^0 and η peaks is already visible in the raw data and background can be drastically reduced to only few percents when also kinematical cuts are imposed.

5 Time request

The overall time planning for the installation and commissioning phase is summarized in Table 3. For mounting of large parts of the apparatus, e.g. dipole magnet and BGO ball, the hall crane is needed. Due to radiation safety this then prohibits any beam

installation & commissioning step	**time period**	**access time (days)**	**test beam time (days)**
basic floor preparation	– Sep/09	15	
beam alignment	Sep/09 – Oct/09	–	2
dipole magnet	Aug/09 – Sep/09	7	
DC x-tracker	Sep/09 – Dec/09	2	3
DC y-, u-, v-tracker lab tests	Sep/09 – Dec/09	–	–
DC y-, u-, v- area inst. & tests	Dec/09 – Mar/10	5	3
SciFi2	Sep/09 – Nov/09	–	3
MOMO	Oct/09 – Nov/09	–	2
Aerogel Cherenkov	Dec/09	–	1
TOF	Apr/10 – May/10	5	2
BGO calorimeter & scintillator barrel	Sep/09 – Apr/10	5	7
Cryogenic LH_2/LD_2 target	Jan/10 – Apr/10	2	2
S-tagger incl. pol. & flux mon.	Jan/10 – Apr/10	2	5
total estimated time:		43	30/20

Table 3: Overview of the planned setup steps and time requirements. Access time does not allow beam in the E-area due to radiation safety requirements. Making use of parallel testing of detector components whenever possible limits the beamtime request to appr. 20 days (see also text).

in the hall. The corresponding access time is estimated in the third column of Table 3. Taking the subdetectors into operation requires short beam tests, usually 1–2 days. The dedicated test beamtime is specified in the last column of Table 3. In order to make efficient use of beamtime resources, testing of detector components in beamline S will be performed in parallel whenever possible and adequate. Hence, the total request of 20 days is significantly less than the sum of the individual detector test times in the rightmost column of Table 3.
Over the period of about one year from now the total time estimate is:

for setup with full hall access (w/o beam) 43 days
for test beamtime 20 days.

The time planning for hall access and beam tests will be made in close cooperation with the Crystal Barrel collaboration. It is the goal to keep interferences with the data taking in beamline E to the absolute minimum.

References

[1] O. Bartalini et al., Nucl. Instr. and Meth **A 562** (2006) 85

[2] I. Jaegle et al., Phys. Rev. Lett. **100** (2008) 252002

[3] R. Di Salvo, Int. J. Mod. Phys. **A 20** (2005) 1918

[4] V. Kuznetsov et al., Phys. Lett. **647** (2007) 23

[5] A. Fantini et al., Phys. Rev. **C 78** (2008) 015203

[6] T. Mart and C. Bennhold, Phys. Rev. **C 61**, 012201 (2000)

[7] C. Bennhold et al., nucl-th/0008024

[8] W.-T. Chiang, F. Tabakin, T.-S.H. Lee, B. Saghai, Phys. Lett. **B 517**, 101 (2001)

[9] A. d'Angelo et al., proceedings of NSTAR2001, ed. by D. Drechsel and L. Tiator, World Scientific (2001), p. 347

[10] A. Lleres et al., Eur. Phys. J. **A 31** (2007) 79

[11] A. Lleres et al., Eur. Phys. J. **A 39** (2009) 149

[12] D. Drechsel, O. Hanstein, S.S. Kamalov and L. Tiator, Nucl. Phys. **A 645**, 145 (1999) and http://www.kph.uni-mainz.de/MAID/kaon/

[13] T. Nakano et al., Phys. Rev. **C 79** (2009) 025210

[14] M.F.M. Lutz and M. Soyeur, Nucl. Phys. **A 748** (2005) 499

[15] B. Borasoy, R. Nissler and W. Weise, Eur. Phys. J. **A 25** (2005) 79

[16] M. Cargnelli et al., Int. J. Mod. Phys. **A 20** (2005) 341

[17] Frank Klein et al., Phys. Rev. **D 78** (2008) 117101

[18] J. Junkersfeld et al., Eur. Phys. J. **A 31** (2007) 365

[19] M. Nanova et al., Eur. Phys. J. **A 35** (2008) 333

[20] S. Penner et al., Phys. Rev. C **66** (2002) 055212, V. Shklyar et al., Phys. Rev. C **71** (2005) 055206 and **72** (2005) 019903

[21] S. Capstick and W. Roberts, Phys. Rev. D **47** (1993) 1994

[22] E. Anciant *et* al., Phys. Rev. Lett. **8**5 (2000) 4682

[23] K. McCormick *et* al., Phys. Rev. C **69** (2004) 032203

[24] J. Barth *et* al., Eur. Phys. J. A **1**7 (2003) 269

[25] T. Mibe *et* al., Phys. Rev. Lett. **9**5 (2005) 182001

[26] T. Mibe *et* al., Phys. Rev. **C 76** (2007) 052202

[27] W. C. Chang *et* al., Phys. Lett. **B 658** (2008) 209

[28] A. I. Titov and B. Kämpfer, Phys. Rev. **C 76** (2007) 035202

[29] Phys. Rev. Lett **100** (2008) 192302

[30] Phys. Rev. Lett **94** (2005) 192303

[31] D. Elsner et al., Eur. Phys. J. **A 39** (2009) 373

[32] F. Bellemann et al., Phys. Rev. **C 60** (1999) 061002

[33] F. Bellemann et al., Phys. Rev. **C 75** (2007) 015204

[34] S. Böse, doctoral thesis, Bonn (in preparation)

[35] S. Materne, diploma thesis, Bonn (2007)

[36] S. Friedrich, diplome thesis, Giessen (2008)

[37] D. Hammann, diploma thesis, Bonn (2008)

[38] R. T. Giles *et al.*, Nucl. Instr. Meth. A **252** (1986) 41

[39] A. Ramseger, diploma thesis, Bonn (2007)

[40] P. Levi Sandri et al., Nucl. Instr. and Meth **A 370** (1996) 396

[41] A. Zucchiatti et al., Nucl. Instr. and Meth **A 321** (1992) 219

[42] M. Anghinolfi et al., Nucl. Instr. and Meth **A 362** (1995) 292

[43] F. Ghio et al., Nucl. Instr. and Meth **A 404** (1998) 71

[44] M. Castoldi et al., Nucl. Instr. and Meth **A 403** (1998) 22

[45] L. Nicoletti, PhD thesis, University of Grenoble, 2002.

[46] G.Audit *et al.*, Nucl.Instr. Meth. A301, 473 (1991).

[47] I.G.Alekseev *et al.* (EPECUR collaboration), arXiv:physics/0701108v1,2007.